electronics

MDPI

Article

Linear-Extended-State-Observer-Based Adaptive RISE Control for the Wrist Joints of Manipulators with Electro-Hydraulic Servo Systems

Junjie Mi, Wenxiang Deng *, Jianyong Yao and Xianglong Liang

School of Mechanical Engineering, Nanjing University of Science and Technology, Nanjing 210094, China; meejj@njust.edu.cn (J.M.); jerryyao.buaa@gmail.com (J.Y.); xlliang.njust@gmail.com (X.L.)
* Correspondence: wxdeng_njust@163.com; Tel.: +86-15705186199

Abstract: Manipulators are multi-rigid-body systems composed of multiple moving joints. During movement, the Coriolis force, centrifugal force, and gravity of the system undergo significant changes. The last three degrees of freedom (DOFs) of the wrist joint of a manipulator control the end attitude. Improving the command tracking accuracy of the wrist joint is a key challenge in controlling the end attitude of manipulators. In this study, a dynamics model of the mechanical arm–wrist joint is established based on the Lagrange method. An adaptive continuous robust integral of the sign of the error (ARISE) controller is designed using the reverse step method. Additionally, a linear extended state observer (LESO) is employed to estimate the time-varying interference existing in the system and compensate for it in the designed control rate. The stability of the Lyapunov function and the boundedness of the observer are proven. The proposed control method for the wrist joint is compared with other controllers on an experimental platform of multi-DOF hydraulic manipulators. The results demonstrate that the proposed method improves the control performance of hydraulic manipulators. The application of this method offers a new strategy and idea for achieving high-performance tracking control in hydraulic manipulators.

Keywords: manipulators; electro-hydraulic servo; nonlinear control; continuous robust integral of the sign of the error (RISE); linear extended state observer (LESO); disturbance compensation; adaptive control

check for updates

Citation: Mi, J.; Deng, W.; Yao, J.; Liang, X. Linear-Extended-State-Observer-Based Adaptive RISE Control for the Wrist Joints of Manipulators with Electro-Hydraulic Servo Systems. *Electronics* **2024**, *13*, 1060. https://doi.org/10.3390/electronics13061060

Academic Editor: Maysam Abbod

Received: 29 December 2023
Revised: 27 February 2024
Accepted: 8 March 2024
Published: 12 March 2024

Copyright: © 2024 by the authors. Licensee MDPI, Basel, Switzerland. This article is an open access article distributed under the terms and conditions of the Creative Commons Attribution (CC BY) license (https://creativecommons.org/licenses/by/4.0/).

1. Introduction

With the continuous development of industrial automation technology, more and more manipulators are applied in production and daily life [1,2], such as aircraft assembly, load handling, and medical assistance [3]. According to the driving form, the manipulators can be roughly divided into two types: electric drive and hydraulic drive. Among them, electric drive robots have played an important role in the development of automation in the past because of their small size and low noise. With the increase in load mass, hydraulically driven manipulators have gradually entered the people's field of vision. Compared to an electric drive transmission, a hydraulic transmission has the advantages of a high power-to-weight ratio, strong anti-interference ability, reliable structure, small volume, and so on. However, because heavy-duty manipulators are currently unable to have as high a positioning accuracy as electrically driven manipulators, they still require more personnel to be involved in very dangerous work in more industrial areas. Therefore, improving the tracking control performance of heavy-duty hydraulic manipulators has become the main way to solve this problem.

In order to realize the complex attitude of the end load of manipulators, the high precision control of the end attitude of 3-DOF wrist joints of manipulators is particularly important. Therefore, how to improve the tracking accuracy of the wrist joints of the mechanical arms has become an urgent problem to be solved.

The application of hydraulic systems can be traced back to 1850 when the United Kingdom began to apply PASCAL's principle to cranes, presses, etc. The real popularity and use of hydraulic systems in industry began after the middle of the 20th century. At the same time, the theory of hydraulic control systems based on valve control was put forward [4], and a large number of studies were conducted on the characteristics of electro-hydraulic servo valves [5–7], especially the saturation characteristics [8] and dead zone [9]. With the development of electro-hydraulic servo technology, such as the application of adaptive control, robust control, sliding mode control, nonlinear friction compensation, and other methods in the field of fluid transmission [10,11], more and more drive forms began to adopt hydraulic drives [12], such as the aerospace rudder actuator, the landing gear retracting mechanism, etc. Finally, the electro-hydrostatic actuator (EHA) was proposed [13,14].

For manipulators with a 6-R (six rotating joint) configuration [15–17], the first three rotating joints (waist, shoulder, and elbow) can make the end reach any position in the 3D working space [18], and the last three rotating joints (wrist) are used to adjust the attitude of the end actuator, which is applicable to application scenarios requiring high-precision control of equal attitude in aerospace. It is not only necessary that the manipulators have excellent spatial positioning ability, but also the tracking and maintaining of the end attitude is particularly important. In recent years, with the development of nonlinear control technology, the control of multi-DOF robotic arms [19] has also attracted the attention of many scholars. However, hydraulically driven robotic arms still have a certain distance for high-precision heavy-duty engineering applications. Among them, the optimization of the control strategy plays a significant role in improving the tracking accuracy of the system.

The proposed linear control strategy has laid a solid foundation for the development of control theory. With the continuous improvement in control performance requirements, nonlinear control strategies are gradually proposed and improved. Since the 1990s, nonlinear algorithms have been rapidly developed, among which the sliding mode control (SMC) [20] has been widely used due to its simple structure, effective handling of uncertainties of any bounded model, and good steady-state tracking accuracy. However, due to the discontinuity of traditional synovial control, many deformation forms of sliding mode control have been derived, among which the higher-order sliding mode control [21,22] method has received extensive attention. Under the condition of increasing complexity of controlled objects, control theory is also being developed. In order to solve the problem that the actual system and controller parameters cannot be accurately known, the adaptive theory is proposed, including direct adaptive and indirect adaptive strategies. Subsequently, the proposed adaptive robust control (ARC) [23–25] has become an effective control strategy for complex controlled objects for a period of time, and the feasibility of the application of this theory on electro-hydraulic servo systems has been verified through experiments, which achieved better control performance. In recent years, a continuous robust integral of the sign of the error (RISE) [26,27] control strategy, based on error symbols, was proposed to deal with model uncertainty by integrating signal feedback terms, and it has been successfully applied to electromechanical and electro-hydraulic servo systems. However, when faced with the limitations of modeling, there is always a certain gap between the real system model and the theoretical model, which leads to the actual tracking performance of the controller not achieving the expected effect. Gradually, some scholars began to study the model errors and disturbance compensation.

The strong coupling between the manipulator joints and the strong nonlinearity of the hydraulic system lead to many complex unmodeled errors and disturbances in the trajectory tracking control process. The proposed observer provides a new way to solve this problem. Under the condition of certain limitations of sensor and measurement technology, the closed-loop observer is constructed by using real system output error feedback correction so that it can accurately observe the real state of the system. The emergence of Luenberger observers solves such problems to a certain extent. With the continuous im-

provement in control accuracy requirements, no matter the traditional linear control theory or nonlinear control theory, when the model-based control strategy is oriented toward complex objects, unmodeled errors and disturbances always exist and cannot be reflected in the model compensation. In order to solve this problem, the extended state observer (ESO) has gradually gained the attention of researchers, including the linear extended state observer (LESO) [28] and the nonlinear extended state observer (NESO) [29]. The basic theory is to treat the error terms and disturbances that cannot be accurately modeled as excessive system states, design an observer by using the error feedback principle, and compensate them in the control algorithm. Thus, the theory of active disturbance rejection control (ADRC) [30–32] is proposed. Many scholars at home and abroad have applied the theory to electro-hydraulic servo systems and verified the feasibility of the method through experiments, which provides a new solution for error and interference compensation. However, this method has not been experimentally verified on multi-DOF hydraulic-driven manipulator systems.

In this study, a mechanical wrist joint dynamics model, considering continuous external disturbances, is established, which improves the modeling accuracy compared with the previous single-joint decomposition control. Compared with 6-DOF whole-arm dynamics modeling, the modeling process is greatly simplified. At the same time, the adaptive theory is combined with the RISE controller design process to design adaptive rates for some parameters of the controller, and uncertainties such as modeling errors and disturbances are estimated through LESO. The asymptotic stability of the system is proved based on the Lyapunov stability theory. This method is first applied to the multi-DOF electro-hydraulic servo manipulator system. Compared with other methods, a better control effect is obtained through experimental comparison and analysis, which provides experimental support and new research ideas for improving the control performance of electro-hydraulic servo manipulators.

The remainder of this article is arranged as follows. In Section 2, a 3-DOF system dynamics model of the wrist joint of the electro-hydraulic servo manipulator is presented considering the uncertainty of matching and mismatching. Section 3 provides the design process of the linear extended state observer. Section 4 provides the detailed design steps of the ARISE controller and the stability of the system. In Section 5, a comparative experimental analysis is carried out based on the experimental platform of an electro-hydraulic servo manipulator with multiple DOFs. Finally, Section 6 summarizes the work of this study and looks forward to future research work.

2. System Models

In this work, the 3-DOF wrist joint of the manipulator is taken as the research object. As shown in Figure 1, each joint of the wrist joint is driven by the electro-hydraulic servo system. The electro-hydraulic servo valve controls the flow required by the hydraulic actuator of each joint, and the joint rotation is controlled by the hydraulic motor so as to complete the task of tracking the command trajectory. The schematic diagram of the motor structure is shown in Figure 1, where 1 and 2 represent the two different chambers of the motor, the different shadows represent the two different vanes that drive the motor to rotate.

In this section, the 3-DOF wrist dynamics model based on the electro-hydraulic servo system is presented, and the wrist state space equation under the simultaneous existence of matching and mismatching uncertainties is established, which provides a theoretical basis for the subsequent controller and observer design.

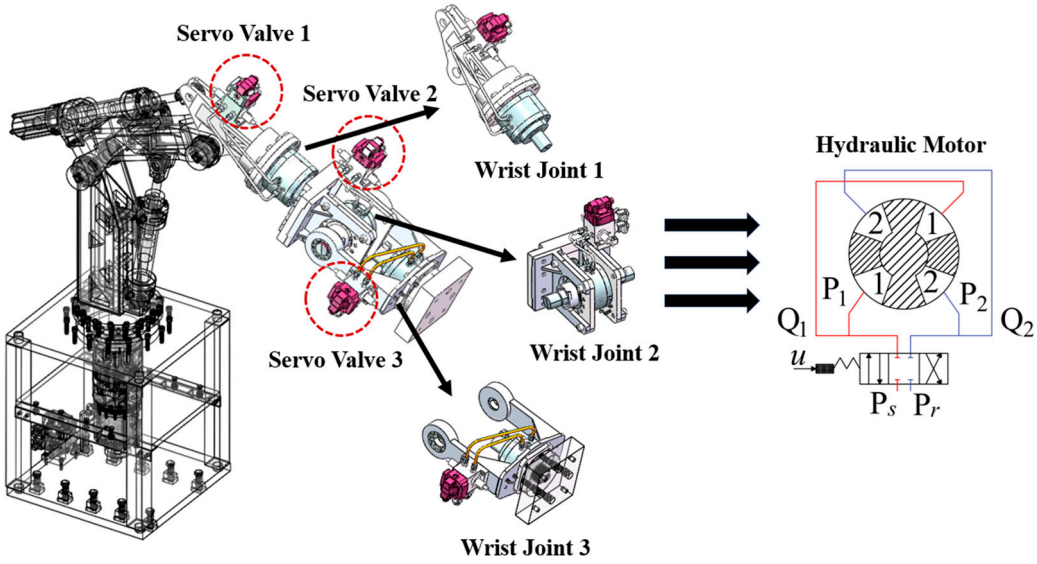


Figure 1. Schematic diagram and actuator of the 3-DOF wrist joint.

2.1. Dynamics of 3-DOF Wrist Joint

The 3-DOF wrist joint dynamics model in joint space can be described as follows:

$$\boldsymbol{M}(\boldsymbol{q})\ddot{\boldsymbol{q}} = \boldsymbol{T} - \boldsymbol{C}(\boldsymbol{q}, \dot{\boldsymbol{q}})\dot{\boldsymbol{q}} - \boldsymbol{G}(\boldsymbol{q}) + \Delta_{t1} \tag{1}$$

where $\boldsymbol{q} = [q_1, q_2, q_3]^T \in \mathbb{R}^3$ is the rotation angle vector, which represents the rotation angle of each joint, and $\dot{\boldsymbol{q}} \in \mathbb{R}^3$ and $\ddot{\boldsymbol{q}} \in \mathbb{R}^3$ are the rotation angular velocity and angular acceleration vectors. $\boldsymbol{M}(\boldsymbol{q}) \in \mathbb{R}^{3\times3}$ is the inertia matrix in the joint space, which is a symmetric matrix where the principal diagonal element M_{jj} describes the inertia of this join, and the joint torque can be expressed as $Q_i = M_{ii}\ddot{q}_i$, $i = 1, 2, 3$, under single joint motion; $\boldsymbol{C}(\boldsymbol{q}, \dot{\boldsymbol{q}}) \in \mathbb{R}^{3\times3}$ is the Coriolis force matrix, including joint angle and velocity vector; $\boldsymbol{G}(\boldsymbol{q}) \in \mathbb{R}^3$ represents the gravity vector, which changes as the joint moves; $\Delta_{t1} = [\Delta_{t11}, \Delta_{t12}, \Delta_{t13}]^T \in \mathbb{R}^3$ is the unmodeled error vector, including the unmodeled dynamics and interference; and $\boldsymbol{T} \in \mathbb{R}^3$ represents the torque required by the joint. Appendix A provides the specific expressions of each matrix and vector in (1).

Assumption 1. *The error term $\Delta_{t1} \in \mathbb{R}^3$ is differentiable at least second order and bounded at the same time, satisfying that $|\Delta_{t1i}| \le \delta_{1i}$, $\left|\dot{\Delta}_{t1i}\right| \le \delta_{2i}$, $\left|\ddot{\Delta}_{t1i}\right| \le \delta_{3i}$, δ_{1i}, δ_{2i}, and δ_{3i} are positive constants.*

2.2. Dynamics of Hydraulic Actuators

As shown in Figure 1, the wrist joint is driven by a two-vane oscillating hydraulic motor, and the flow rate is controlled by a servo valve to achieve the command trajectory tracking task. In order to not lose generality, the pressure dynamics of each wrist shutdown hydraulic motor can be expressed as:

$$\begin{cases} \dot{P}_{1i} = \beta_e V_{1i}^{-1}\left(Q_{1i} - D_{mi}\dot{q}_i - C_t(P_1 - P_2)\right) + d_{1i}(t) \\ \dot{P}_{2i} = \beta_e V_{2i}^{-1}\left(-Q_{2i} - D_{mi}\dot{q}_i + C_t(P_1 - P_2)\right) - d_{2i}(t) \end{cases} \tag{2}$$

where $i = 1, 2, 3$ stands for every joint; β_e represents the elastic modulus of hydraulic oil, which is a constant value; $V_{1i} = V_{01i} + D_{m1i}\dot{q}_i$ and $V_{2i} = V_{02i} + D_{m2i}\dot{q}_i$ represent the volume of the oil chamber of the hydraulic motor; and V_{01i} and V_{02i} represent the initial volume of the oil cavity. Q_{1i} and Q_{2i} are the inlet and return flow rates of the two oil cavities, where Q_{1i} is a positive representation of the inlet of oil in chamber 1, Q_{1i} is a negative representation of the return of oil in chamber 1, and Q_{2i} is opposite. D_{mi} represents the effective

volume of a two-chamber blade per unit angle, and $d_{1i}(t)$ and $d_{2i}(t)$ represent unmodeled error terms in the two chambers, including but not limited to unmodeled internal and external leaks.

The pressure dynamics of each joint can be expressed in vector form as:

$$\begin{cases} \dot{\boldsymbol{P}}_1 = \left[\dot{P}_{11}, \dot{P}_{12}, \dot{P}_{13}\right]^T \in \mathbb{R}^3 \\ \dot{\boldsymbol{P}}_2 = \left[\dot{P}_{21}, \dot{P}_{22}, \dot{P}_{23}\right]^T \in \mathbb{R}^3 \end{cases} \tag{3}$$

Since each joint is independently controlled by each servo valve, the valve port characteristics of the servo valve itself cannot be ignored. The spool displacement $x_{ui} = k_{ui}u_i$ is proportional to the control output u_i. The two-chamber flow equation can be written as:

$$\begin{cases} Q_{1i} = k_{qi}k_{ui}u_i\left(s(u_i)\sqrt{P_{si} - P_{1i}} + s(-u_i)\sqrt{P_{1i} - P_{ri}}\right) \\ Q_{2i} = k_{qi}k_{ui}u_i\left(s(u_i)\sqrt{P_{2i} - P_{ri}} + s(-u_i)\sqrt{P_{si} - P_{2i}}\right) \end{cases} \tag{4}$$

where $k_{qi} = C_{di}\omega_i\sqrt{2/\rho}$ is a positive constant, C_{di} represents the servo valve flow coefficient, ω_i represents the spool area gradient, ρ represents the hydraulic oil density, and P_{si} and P_{ri} represent the inlet and return oil pressures, respectively.

Define the symbolic function $s(*)$ as follows:

$$s(*) = \begin{cases} 1, \text{ if } * \geq 0 \\ 0 \text{ if } * < 0 \end{cases} \tag{5}$$

The actual output torque of each joint hydraulic motor is expressed as:

$$\boldsymbol{T} = \boldsymbol{D_m}(\boldsymbol{P}_1 - \boldsymbol{P}_2) \in \mathbb{R}^3 \tag{6}$$

where

$$\begin{aligned} \boldsymbol{D_m} &= \text{diag}\{D_{m1}, D_{m2}, D_{m3}\} \in \mathbb{R}^{3\times3} \\ \boldsymbol{P}_1 &= [P_{11}, P_{12}, P_{13}]^T \in \mathbb{R}^3 \\ \boldsymbol{P}_2 &= [P_{21}, P_{22}, P_{23}]^T \in \mathbb{R}^3 \end{aligned} \tag{7}$$

2.3. State Space Model

Define the state variable as follows:

$$\boldsymbol{x} = \left[\boldsymbol{x}_1^T, \boldsymbol{x}_2^T, \boldsymbol{x}_3^T\right]^T \in \mathbb{R}^9 \tag{8}$$

where $\boldsymbol{x}_1 = \boldsymbol{q}$, $\boldsymbol{x}_2 = \dot{\boldsymbol{q}}$, $\boldsymbol{x}_3 = (\boldsymbol{P}_1 - \boldsymbol{P}_2)$.

According to (1), (2), (4), (6), and (8), the electrohydraulic servo wrist state space equation can be formulated in the following form:

$$\begin{cases} \dot{\boldsymbol{x}}_1 = \boldsymbol{x}_2 \\ \dot{\boldsymbol{x}}_2 = \boldsymbol{M}^{-1}(\boldsymbol{x}_1)[\boldsymbol{D}_m\boldsymbol{x}_3 - \boldsymbol{C}(\boldsymbol{x}_1, \boldsymbol{x}_2)\boldsymbol{x}_2 - \boldsymbol{G}(\boldsymbol{x}_1) + \Delta_{t1}] \\ \dot{\boldsymbol{x}}_3 = \boldsymbol{f}_1\boldsymbol{u} - \boldsymbol{f}_2 - \boldsymbol{f}_3 + \Delta_{t2} \end{cases} \tag{9}$$

$$\begin{cases} \boldsymbol{f}_1 \triangleq \beta_e\boldsymbol{k_t}\left(\boldsymbol{V}_1^{-1}\boldsymbol{R}_1 + \boldsymbol{V}_2^{-1}\boldsymbol{R}_2\right) \\ \boldsymbol{f}_2 \triangleq \beta_e\boldsymbol{D_m}\left(\boldsymbol{V}_1^{-1} + \boldsymbol{V}_2^{-1}\right)\boldsymbol{x}_2 \\ \boldsymbol{f}_2 \triangleq \beta_e\boldsymbol{C_t}\left(\boldsymbol{V}_1^{-1} + \boldsymbol{V}_2^{-1}\right)\boldsymbol{x}_3 \end{cases} \tag{10}$$

where, the parameter of (10) $k_{ti} = k_{qi}k_{ui}$, $\boldsymbol{k_t} = \text{diag}\{k_{t1}, k_{t2}, k_{t3}\} \in \mathbb{R}^{3\times3}$, $\boldsymbol{V}_1 = \text{diag}\{V_{11}, V_{12}, V_{13}\}$, $\boldsymbol{V}_2 = \text{diag}\{V_{21}, V_{22}, V_{23}\} \in \mathbb{R}^{3\times3}$, $\boldsymbol{d}_1(\boldsymbol{t}) = [d_{11}(t), d_{12}(t), d_{13}(t)]^T \in \mathbb{R}^3$, $\boldsymbol{d}_2(\boldsymbol{t}) = [d_{21}(t), d_{22}(t), d_{23}(t)]^T \in \mathbb{R}^3$,

$\Delta_{t2} = \boldsymbol{d}_1 - \boldsymbol{d}_2 \in \mathbb{R}^3$, $\boldsymbol{R}_1 = \mathrm{diag}\{R_{11}, R_{12}, R_{13}\} \in \mathbb{R}^{3\times3}$, $\boldsymbol{R}_2 = \mathrm{diag}\{R_{21}, R_{22}, R_{23}\} \in \mathbb{R}^{3\times3}$, and the specific expression is:

$$\begin{cases} R_{1i} \triangleq s(u_i)\sqrt{P_{si} - P_{1i}} + s(-u_i)\sqrt{P_{1i} - P_{ri}} \\ R_{2i} \triangleq s(u_i)\sqrt{P_{2i} - P_{ri}} + s(-u_i)\sqrt{P_{si} - P_{2i}} \end{cases} \tag{11}$$

Assumption 2. *The error term $\Delta_{t2} \in \mathbb{R}^3$ is differentiable at least second order and bounded at the same time, satisfying that $|\Delta_{t2i}| \le \vartheta_{1i}$, $\left|\dot{\Delta}_{t2i}\right| \le \vartheta_{2i}$, $\left|\ddot{\Delta}_{t2i}\right| \le \vartheta_{3i}$, ϑ_{1i}, ϑ_{2i}, and ϑ_{3i} are positive constants.*

3. Linear Extended State Observer Design

ESO is designed not only to observe system states but also to estimate model uncertainties and perturbations and compensate them during controller design. Before designing the ESO, first define the extended system state as follows:

$$\begin{cases} \boldsymbol{x}_{e1} = \boldsymbol{M}^{-1}\Delta_{t1} \in \mathbb{R}^3 \\ \boldsymbol{x}_{e2} = \Delta_{t2} \in \mathbb{R}^3 \end{cases} \tag{12}$$

$$\begin{cases} \dot{\boldsymbol{x}}_{e1} = \Theta_1(\boldsymbol{t}) \in \mathbb{R}^3 \\ \dot{\boldsymbol{x}}_{e2} = \Theta_2(\boldsymbol{t}) \in \mathbb{R}^3 \end{cases} \tag{13}$$

where $\boldsymbol{x}_{e1}$, $\boldsymbol{x}_{e2}$, $\dot{\boldsymbol{x}}_{e1}$, and $\dot{\boldsymbol{x}}_{e2}$ are bounded.

Combined with (12) and (13), the state space Equation (9) can be redescribed as:

$$\begin{cases} \dot{\boldsymbol{x}}_1 = \boldsymbol{x}_2 \\ \dot{\boldsymbol{x}}_2 = \boldsymbol{M}^{-1}(\boldsymbol{x}_1)[\boldsymbol{D}_m\boldsymbol{x}_3 - \boldsymbol{C}(\boldsymbol{x}_1, \boldsymbol{x}_2)\boldsymbol{x}_2 - \boldsymbol{G}(\boldsymbol{x}_1)] + \boldsymbol{x}_{e1} \\ \dot{\boldsymbol{x}}_3 = \boldsymbol{f}_1\boldsymbol{u} - \boldsymbol{f}_2 - \boldsymbol{f}_3 + \boldsymbol{x}_{e2} \end{cases} \tag{14}$$

According to (14), the ESO structure can be expressed as:

$$\begin{cases} \dot{\hat{\boldsymbol{x}}}_1 = \hat{\boldsymbol{x}}_2 + 3\boldsymbol{w}_{e1}(\boldsymbol{x}_1 - \hat{\boldsymbol{x}}_1) \\ \dot{\hat{\boldsymbol{x}}}_2 = \boldsymbol{M}^{-1}(\boldsymbol{x}_1)[\boldsymbol{D}_m\boldsymbol{x}_3 - \boldsymbol{C}(\boldsymbol{x}_1, \boldsymbol{x}_2)\boldsymbol{x}_2 - \boldsymbol{G}(\boldsymbol{x}_1)] + \\ \quad \hat{\boldsymbol{x}}_{e1} + 3\boldsymbol{w}_{e1}^2(\boldsymbol{x}_1 - \hat{\boldsymbol{x}}_1) \\ \dot{\hat{\boldsymbol{x}}}_{e1} = \boldsymbol{w}_{e1}^3(\boldsymbol{x}_1 - \hat{\boldsymbol{x}}_1) \end{cases} \tag{15}$$

$$\begin{cases} \dot{\hat{\boldsymbol{x}}}_3 = \boldsymbol{f}_1\boldsymbol{u} - \boldsymbol{f}_2 - \boldsymbol{f}_3 + \hat{\boldsymbol{x}}_{e2} + 2\boldsymbol{w}_{e2}(\boldsymbol{x}_3 - \hat{\boldsymbol{x}}_3) \\ \dot{\hat{\boldsymbol{x}}}_{e2} = \boldsymbol{w}_{e2}^2(\boldsymbol{x}_3 - \hat{\boldsymbol{x}}_3) \end{cases} \tag{16}$$

where $\hat{x}_i$ represents the estimate of x_i, and $\boldsymbol{w}_{\mathrm{ei}} = \mathrm{diag}\{w_{ei1}, w_{ei2}, w_{ei3}\} \in \mathbb{R}^{3\times3}$ are positive constants that determine the ESO bandwidth and the observed effect.

The state observation error of ESO is defined as $\tilde{\bullet} = \bullet - \hat{\bullet}$. From (12) to (16), the estimation error dynamics of state variables can be described as:

$$\begin{cases} \dot{\tilde{\boldsymbol{x}}}_1 = \tilde{\boldsymbol{x}}_2 - 3\boldsymbol{w}_{e1}\tilde{\boldsymbol{x}}_1 \\ \dot{\tilde{\boldsymbol{x}}}_2 = \tilde{\boldsymbol{x}}_{e1} - 3\boldsymbol{w}_{e1}^2\tilde{\boldsymbol{x}}_1 \\ \dot{\tilde{\boldsymbol{x}}}_{e1} = \Theta_1(\boldsymbol{t}) - \boldsymbol{w}_{e1}^3\tilde{\boldsymbol{x}}_1 \end{cases} \tag{17}$$

$$\begin{cases} \dot{\tilde{\boldsymbol{x}}}_3 = \tilde{\boldsymbol{x}}_{e2} - 2\boldsymbol{w}_{e2}\tilde{\boldsymbol{x}}_3 \\ \dot{\tilde{\boldsymbol{x}}}_{e2} = \Theta_2(\boldsymbol{t}) - \boldsymbol{w}_{e2}^2\tilde{\boldsymbol{x}}_3 \end{cases} \tag{18}$$

In order to facilitate the subsequent ESO stability analysis, the estimated error vector is designed as $\varepsilon_1 = [\varepsilon_{11}, \varepsilon_{12}, \varepsilon_{13}]^T = [\tilde{\boldsymbol{x}}_1, \boldsymbol{w}_{e1}^{-1}\tilde{\boldsymbol{x}}_2, \boldsymbol{w}_{e1}^{-2}\tilde{\boldsymbol{x}}_{e1}]^T \in \mathbb{R}^9$, $\varepsilon_2 = [\varepsilon_{21}, \varepsilon_{22}]^T =$

$[\tilde{x}_2, w_{e2}^{-1}\tilde{x}_{e2}]^T \in \mathbb{R}^6$. Therefore, the estimation error dynamics in Equations (17) and (18) can be rewritten as follows:

$$\begin{aligned} \dot{\varepsilon}_1 &= w_1(A_1\varepsilon_1) + B_1 w_1^{-2} H_1(t) \\ \dot{\varepsilon}_2 &= w_2(A_2\varepsilon_2) + B_2 w_2^{-1} H_2(t) \end{aligned} \tag{19}$$

$$\begin{cases} w_1 = \begin{bmatrix} w_{e1} & & \\ & w_{e1} & \\ & & w_{e1} \end{bmatrix} \in \mathbb{R}^{9\times 9} \\ A_1 = \begin{bmatrix} -3I_3 & I_3 & 0_3 \\ -3I_3 & 0_3 & I_3 \\ -I_3 & 0_3 & 0_3 \end{bmatrix} \in \mathbb{R}^{9\times 9} \\ B_1 = \begin{bmatrix} 0_3 & & \\ & 0_3 & \\ & & I_3 \end{bmatrix} \in \mathbb{R}^{9\times 9}, H_1(t) = \begin{bmatrix} 0_3 \\ 0_3 \\ \Theta_1(t) \end{bmatrix} \in \mathbb{R}^9 \end{cases} \tag{20}$$

$$\begin{cases} w_2 = \begin{bmatrix} w_{e2} & \\ & w_{e2} \end{bmatrix} \in \mathbb{R}^{6\times 6}, A_2 = \begin{bmatrix} -2I_3 & I_3 \\ -I_3 & 0_3 \end{bmatrix} \in \mathbb{R}^{6\times 6} \\ B_2 = \begin{bmatrix} 0_3 & \\ & I_3 \end{bmatrix} \in \mathbb{R}^{6\times 6}, H_2(t) = \begin{bmatrix} 0_3 \\ \Theta_2(t) \end{bmatrix} \in \mathbb{R}^6 \end{cases} \tag{21}$$

where $I_3 \in \mathbb{R}^{3\times 3}$ represents the identity matrix; $0_3 \in \mathbb{R}^{3\times 3}$ stands for zero matrix; and $A_1 \in \mathbb{R}^{9\times 9}$ and $A_2 \in \mathbb{R}^{6\times 6}$ are the Hurwitz matrices, so there are positive definite matrices $N_1 \in \mathbb{R}^{9\times 9}$ and $N_2 \in \mathbb{R}^{6\times 6}$ that satisfy $A_1^T N_1 + N_1 A_1 = -2I_9$ and $A_2^T N_2 + N_2 A_2 = -2I_6$.

4. Controller Design

4.1. RISE-Based Controller Design

The design process of the controller is based on the backstepping technique. Combined with the system state estimation designed by using the ESO, the uncertainty of matching and mismatching was compensated during the controller design process.

Design error and auxiliary error variables are shown below:

$$\begin{aligned} e_1 &= x_1 - x_{1d} \in \mathbb{R}^3, \quad & r_1 &= \dot{e}_2 + k_2 e_2 \in \mathbb{R}^3 \\ e_2 &= \dot{e}_1 + k_1 e_1 \in \mathbb{R}^3, \quad & r_2 &= \dot{e}_3 + k_3 e_3 \in \mathbb{R}^3 \\ e_3 &= x_3 - \alpha_2 \in \mathbb{R}^3 \end{aligned} \tag{22}$$

where $k_i = \mathrm{diag}\{k_{i1}, k_{i2}, k_{i3}\}$ are positive constant matrices and $\alpha_2 \in \mathbb{R}^3$ stands for the virtual control rate.

According to (14) and (22), the following may be obtained:

$$M(x_1)r_1 = E + F_n + M(x_1)x_{e1} + D_m(e_3 + \alpha_2) \tag{23}$$

$$E = M(x_1)\left(k_1\dot{e}_1 + k_2 e_2\right) \tag{24}$$

$$F_n = -\left[C(x_1, x_2)x_2 + G(x_1) + M(x_1)\ddot{x}_{1d}\right] \tag{25}$$

Combined with (23)–(25), the virtual control rate α_2 is designed as:

$$\begin{aligned} \alpha_2 &= {D_m}^{-1}(\alpha_{2a} + \alpha_{2s1} + \alpha_{2s2}) \\ \alpha_{2a} &= -F_n - M(x_1)\hat{x}_{e1} \\ \alpha_{2s1} &= -(k_{r1} + k_s)e_2 - E \\ \alpha_{2s2} &= -\int_0^t [(k_{r1} + k_s)k_2 e_2 + \beta_1 \mathrm{sign}(e_2)] \end{aligned} \tag{26}$$

where $k_s = \mathrm{diag}\{k_{s1}, k_{s2}, k_{s3}\}$, $k_{r1} = \mathrm{diag}\{k_{r11}, k_{r12}, k_{r13}\}$, and $\beta_1 = [\beta_{11}, \beta_{12}, \beta_{13}]^T$ are positive constant matrices; $\alpha_{2a} \in \mathbb{R}^3$ represents the model compensation term to compensate for the known modeling part; $\alpha_{2s1} \in \mathbb{R}^3$ stands for the linear feedback term; and $\alpha_{2s2} \in \mathbb{R}^3$ stands for the RISE feedback term, tuning state estimation error, and interference.

The symbolic function sign$(*)$ is defined as:

$$\text{sign}(*) = \begin{cases} 1, \text{ if } * > 0 \\ 0, \text{ if } * = 0 \\ -1, \text{ if } * < 0 \end{cases} \tag{27}$$

Substitute (26) into (23) and differentiate to obtain the following:

$$\begin{gathered} \boldsymbol{M}(\boldsymbol{x}_1)\dot{\boldsymbol{r}}_1 = -\dot{\boldsymbol{M}}(\boldsymbol{x}_1)\boldsymbol{r}_1 - (\boldsymbol{k}_{r1} + \boldsymbol{k}_s)\boldsymbol{r}_1 - \boldsymbol{\beta}_1 \text{sign}(\boldsymbol{e}_2) + \boldsymbol{D}_m\dot{\boldsymbol{e}}_3 + \\ \dot{\boldsymbol{M}}(\boldsymbol{x}_1)\tilde{\boldsymbol{x}}_{e1} + \boldsymbol{M}(\boldsymbol{x}_1)\dot{\tilde{\boldsymbol{x}}}_{e1} \end{gathered} \tag{28}$$

Combining (14), (16), and (22), the auxiliary error vector can be described as:

$$\boldsymbol{r}_2 = \boldsymbol{f}_1\boldsymbol{u} - \boldsymbol{f}_2 - \boldsymbol{f}_3 + \boldsymbol{x}_{e2} - \dot{\boldsymbol{\alpha}}_2 + \boldsymbol{k}_3\boldsymbol{e}_3 \tag{29}$$

According to (3), the control rate can be designed as follows:

$$\begin{aligned} &\boldsymbol{u} = \boldsymbol{f}_1{}^{-1}(\boldsymbol{u}_a + \boldsymbol{u}_{s1} + \boldsymbol{u}_{s2}) \\ &\boldsymbol{u}_a = \dot{\alpha}_2 + f_2 + f_3 - k_3e_3 - \hat{\boldsymbol{x}}_{e2} \\ &\boldsymbol{u}_{s1} = -\boldsymbol{k}_{r2}\boldsymbol{e}_3 \\ &\boldsymbol{u}_{s2} = -\int_0^t [\boldsymbol{k}_{r2}\boldsymbol{k}_3\boldsymbol{e}_3 + \boldsymbol{\beta}_2 \text{sign}(\boldsymbol{e}_3)]d\tau \end{aligned} \tag{30}$$

where $\boldsymbol{u} \in \mathbb{R}^3$, $\boldsymbol{k}_{r2} = \text{diag}\{k_{r21}, k_{r22}, k_{r23}\}$, $\boldsymbol{\beta}_2 = [\beta_{21}, \beta_{22}, \beta_{23}]^T \in \mathbb{R}^3$; $\boldsymbol{u}_a$ represents the model compensation term to compensate for the modeled part of the electro-hydraulic servo system; $\boldsymbol{u}_{s1}$ represents the linear robust feedback term to tune the system; and $\boldsymbol{u}_{s2}$ represents the RISE feedback term to deal with various model uncertainties.

Substitute (30) into (29) to obtain the following:

$$\dot{\boldsymbol{r}}_2 = -\boldsymbol{k}_{r2}\boldsymbol{r}_2 - \boldsymbol{\beta}_2 \text{sign}(\boldsymbol{e}_3) + \dot{\tilde{\boldsymbol{x}}}_{e2} \tag{31}$$

4.2. Adaptive Law Design of Controller Parameters

With the increase in degrees of freedom, the proportion of joint coupling dynamics and unmodeled uncertainties in the dynamics model of manipulator systems will increase greatly, which results in a model with strong uncertainties, hindering the tracking accuracy of manipulator joints, and making the adjustment of controller parameters a very difficult process. Therefore, this section introduces the adaptive theory to design the adaptive law and realize the self-tuning of some parameters of the controller.

Combined with adaptive theory, Equations (26) and (30) can be redescribed as:

$$\boldsymbol{\alpha}_{2s2} = -\int_0^t \left[(\boldsymbol{k}_{r1} + \boldsymbol{k}_s)\boldsymbol{k}_2\boldsymbol{e}_2 + \hat{\boldsymbol{\beta}}_1 \text{sign}(\boldsymbol{e}_2) \right] d\tau \tag{32}$$

$$\boldsymbol{u}_{s2} = -\int_0^t \left[\boldsymbol{k}_{r2}\boldsymbol{k}_3\boldsymbol{e}_3 + \hat{\boldsymbol{\beta}}_2 \text{sign}(\boldsymbol{e}_3) \right] d\tau \tag{33}$$

where $\hat{\boldsymbol{\beta}}_i = \left[\hat{\beta}_{i1}, \hat{\beta}_{i2}, \hat{\beta}_{i3}\right]^T \in \mathbb{R}^3$ represent the estimates of the controller parameters.

The estimated errors of the controller parameters are defined as $\tilde{*} = \hat{*} - *$. The parameter adaptive rate can be designed as follows:

$$\dot{\hat{\beta}}_{1i} = \text{Proj}_{\hat{\beta}_{1i}}[\boldsymbol{\Gamma}_{1i}r_{1i}\text{sign}(e_{2i})] \tag{34}$$

$$\dot{\hat{\beta}}_{2i} = \text{Proj}_{\hat{\beta}_{2i}}[\boldsymbol{\Gamma}_{2i}r_{2i}\text{sign}(e_{3i})] \tag{35}$$

where $\boldsymbol{\Gamma}_i = \text{diag}\{\Gamma_{i1}, \Gamma_{i2}, \Gamma_{i3}\}$ represents the adaptive regression rate of the parameters, and the $\text{Proj}_*(\bullet)$ function ensures that the estimates of the parameters are within the set

value range, $\beta_{ji} \in \left\{\beta_{ji} \middle| \beta_{ji\min} \leq \beta_{ji} \leq \beta_{ji\max}\right\}$, $j = 1, 2$, and $i = 1, 2, 3$. The specific expression of the $\mathrm{Proj}_*(\bullet)$ function is as follows:

$$\mathrm{Proj}_*(\bullet) \triangleq \begin{cases} 0, \text{ if } * = *_{\max} \text{ and } \bullet > 0 \\ 0, \text{ if } * = *_{\min} \text{ and } \bullet < 0 \\ \bullet, \text{ otherwise} \end{cases} \tag{36}$$

where $*$ represents the parameter being adapted and $\bullet$ represents the adaptation law of this parameter. If $*$ reaches the set maximum value and at the same time its adaptive law $\bullet$ is greater than zero, then the adaptive law $\bullet$ of $*$ will be equal to zero and the value of $*$ will not change anymore.

4.3. Stability Analysis

Before the system stability analysis, the design aid equations $L_1(t)$, $L_2(t)$, $\psi_1(t)$, and $\psi_2(t)$ are formulated as follows:

$$L_1(t) \triangleq \boldsymbol{r}_1^T \left[\boldsymbol{M}\dot{\tilde{\boldsymbol{x}}}_{e1} - \boldsymbol{\beta}_1 \mathrm{sign}(\boldsymbol{e}_2)\right] \tag{37}$$

$$L_2(t) \triangleq \boldsymbol{r}_2^T \left[\dot{\tilde{\boldsymbol{x}}}_{e2} - \boldsymbol{\beta}_2 \mathrm{sign}(\boldsymbol{e}_3)\right] \tag{38}$$

$$\psi_1(t) \triangleq \|\boldsymbol{e}_2(0)\|_1 \boldsymbol{\beta}_1 - \boldsymbol{e}_2^T(0)\dot{\Delta}_{t1}(0) - \int_0^t L_1(\tau)d\tau \tag{39}$$

$$\psi_2(t) \triangleq \|\boldsymbol{e}_3(0)\|_1 \boldsymbol{\beta}_2 - \boldsymbol{e}_3^T(0)\dot{\Delta}_{t2}(0) - \int_0^t L_2(\tau)d\tau \tag{40}$$

Combining Assumption 1 and Assumption 2, the elements in Equations (39) and (40) are positive when the controller gain meets the following conditions:

$$\beta_{1i} > \delta_{2i} + \frac{\delta_{3i}}{k_{2i}} \tag{41}$$

$$\beta_{2i} > \vartheta_{2i} + \frac{\vartheta_{3i}}{k_{3i}} \tag{42}$$

In order to verify the global stability of the system, the positive definite Lyapunov function was designed in the following form:

$$\begin{aligned} V(t) \quad \triangleq\ & \tfrac{1}{2}\boldsymbol{e}_1^T\boldsymbol{e}_1 + \tfrac{1}{2}\boldsymbol{e}_2^T\boldsymbol{e}_2 + \tfrac{1}{2}\boldsymbol{e}_3^T\boldsymbol{e}_3 + \tfrac{1}{2}\boldsymbol{r}_1^T\boldsymbol{M}(\boldsymbol{x}_1)\boldsymbol{r}_1 + \tfrac{1}{2}\boldsymbol{r}_2^T\boldsymbol{r}_2 + \\ & \tfrac{1}{2}\widetilde{\boldsymbol{\beta}}_1^T\boldsymbol{\Gamma}_1^{-1}\widetilde{\boldsymbol{\beta}}_1 + \tfrac{1}{2}\widetilde{\boldsymbol{\beta}}_2^T\Gamma_2^{-1}\widetilde{\boldsymbol{\beta}}_2 + \psi_1 + \psi_2 + \tfrac{1}{2}\boldsymbol{\varepsilon}_1^T\boldsymbol{N}_1\boldsymbol{\varepsilon}_1 + \tfrac{1}{2}\boldsymbol{\varepsilon}_2^T\boldsymbol{N}_2\boldsymbol{\varepsilon}_2 \end{aligned} \tag{43}$$

Combining (22), (29), (31), and (34)–(40), the differential form of Equation (43) can be expressed as:

$$\begin{aligned} \dot{V}(t) \quad \triangleq\ & \boldsymbol{e}_1^T(\boldsymbol{e}_2 - \boldsymbol{k}_1\boldsymbol{e}_1) + \boldsymbol{e}_2^T(\boldsymbol{r}_1 - \boldsymbol{k}_2\boldsymbol{e}_2) + \boldsymbol{e}_3^T(\boldsymbol{r}_2 - \boldsymbol{k}_3\boldsymbol{e}_3) + \\ & \boldsymbol{r}_1^T\left[-\dot{\boldsymbol{M}}\boldsymbol{r}_1 - \boldsymbol{k}_{r1}\boldsymbol{r}_1 - \boldsymbol{k}_s\boldsymbol{r}_1 - \ \hat{\boldsymbol{\beta}}_1 \mathrm{sign}(\boldsymbol{e}_2) + \boldsymbol{D}_m\dot{\boldsymbol{e}}_3 + \dot{\boldsymbol{M}}\dot{\tilde{\boldsymbol{x}}}_{e1} + \boldsymbol{M}\ddot{\tilde{\boldsymbol{x}}}_{e1}\right] + \\ & \boldsymbol{r}_2^T\left[-\boldsymbol{k}_{r1}\boldsymbol{r}_2 - \hat{\boldsymbol{\beta}}_2 \mathrm{sign}(\boldsymbol{e}_3) + \dot{\tilde{\boldsymbol{x}}}_{e2}\right] + \\ & \tfrac{1}{2}\boldsymbol{r}_1^T\dot{\boldsymbol{M}}\boldsymbol{r}_1 + \widetilde{\boldsymbol{\beta}}_1^T\boldsymbol{r}_1 \mathrm{sign}(\boldsymbol{e}_2) + \widetilde{\boldsymbol{\beta}}_2^T\boldsymbol{r}_2 \mathrm{sign}(\boldsymbol{e}_3) - \\ & \boldsymbol{r}_1^T\left[\boldsymbol{M}\dot{\tilde{\boldsymbol{x}}}_{e1} - \boldsymbol{\beta}_1 \mathrm{sign}(\boldsymbol{e}_2)\right] - \boldsymbol{r}_2^T\left[\dot{\tilde{\boldsymbol{x}}}_{e2} - \boldsymbol{\beta}_2 \mathrm{sign}(\boldsymbol{e}_3)\right] \end{aligned} \tag{44}$$

Meanwhile, the following variables are defined as:

$$\begin{aligned} & \Delta \triangleq -\tfrac{1}{2}\dot{\boldsymbol{M}}\boldsymbol{r}_1 \leq v(\|\boldsymbol{e}\|)\|\boldsymbol{e}\| \\ & \boldsymbol{e}(t) \triangleq [\boldsymbol{e}_1, \boldsymbol{e}_2, \boldsymbol{e}_3, \boldsymbol{r}_1, \boldsymbol{r}_2]^T \in \mathbb{R}^{15} \end{aligned} \tag{45}$$

where $v(*)$ represents a globally invertible non-decreasing function, combined with Young's inequality:

$$ab \leq \frac{a^p}{p} + \frac{b^q}{q}, \text{ if } \frac{1}{p} + \frac{1}{q} = 1 \tag{46}$$

Equation (46) can be rewritten as follows:

$$\begin{aligned} \dot{V}(t) \leq & -\boldsymbol{e}^T \boldsymbol{\Lambda} \boldsymbol{e} - \boldsymbol{r}_1^T \boldsymbol{k}_s \boldsymbol{r}_1 + \boldsymbol{r}_1^T \dot{\boldsymbol{M}} \boldsymbol{r}_1 - \boldsymbol{\varepsilon}_1^T \boldsymbol{w}_1 \boldsymbol{\varepsilon}_1 - \boldsymbol{\varepsilon}_2^T \boldsymbol{w}_2 \boldsymbol{\varepsilon}_2 + \\ & \frac{1}{2}\|\boldsymbol{\varepsilon}_1\|^2 + \frac{1}{2}\|\boldsymbol{\varepsilon}_2\|^2 + \frac{1}{2}\left\|\boldsymbol{N}_1 \boldsymbol{B}_1 \boldsymbol{w}_1^{-2} \boldsymbol{H}_1\right\|^2 + \frac{1}{2}\left\|\boldsymbol{N}_2 \boldsymbol{B}_2 \boldsymbol{w}_2^{-1} \boldsymbol{H}_2\right\|^2 \end{aligned} \tag{47}$$

where the specific expression of the $\boldsymbol{\Lambda} \in \mathbb{R}^{15\times15}$ matrix is in the following form:

$$\boldsymbol{\Lambda} = \begin{bmatrix} \boldsymbol{k}_1 & -\frac{\boldsymbol{I}_3}{2} & 0_3 & 0_3 & 0_3 \\ -\frac{\boldsymbol{I}_3}{2} & \boldsymbol{k}_2 & 0_3 & -\frac{\boldsymbol{I}_3}{2} & 0_3 \\ 0_3 & 0_3 & \boldsymbol{k}_3 & -\frac{\boldsymbol{D}_m \boldsymbol{k}_3}{2} & -\frac{\boldsymbol{I}_3}{2} \\ 0_3 & -\frac{\boldsymbol{I}_3}{2} & -\frac{\boldsymbol{D}_m \boldsymbol{k}_3}{2} & \boldsymbol{k}_{r1} & -\frac{\boldsymbol{D}_m}{2} \\ 0_3 & 0_3 & -\frac{\boldsymbol{I}_3}{2} & -\frac{\boldsymbol{D}_m}{2} & \boldsymbol{k}_{r2} \end{bmatrix} \tag{48}$$

In (48), by selecting the appropriate elements of the controller gain matrix, $\boldsymbol{k}_1$, $\boldsymbol{k}_2$, $\boldsymbol{k}_3$, $\boldsymbol{k}_{r1}$, and $\boldsymbol{k}_{r2}$, $\Lambda \in \mathbb{R}^{15\times15}$ can always be a positive definite matrix. Thus, Equation (47) can be redescribed as the following inequality:

$$\begin{aligned} \dot{V}(t) \quad & \leq -\lambda_{\min}(\boldsymbol{\Lambda})\|\boldsymbol{e}\|^2 - \lambda_{\min}(\boldsymbol{k}_s)\|\boldsymbol{r}_1\|^2 + v(\|\boldsymbol{e}\|)\|\boldsymbol{e}\|\|\boldsymbol{r}_1\| \\ & -\lambda_{\min}(\boldsymbol{w}_1)\|\boldsymbol{\varepsilon}_1\|^2 - \lambda_{\min}(\boldsymbol{w}_2)\|\boldsymbol{\varepsilon}_2\|^2 \\ & \leq -\left(\lambda_{\min}(\boldsymbol{\Lambda}) + \frac{\lambda_{\min}(\boldsymbol{w}_1)\|\boldsymbol{\varepsilon}_1\|^2}{\|\boldsymbol{e}\|^2} + \frac{\lambda_{\min}(\boldsymbol{w}_2)\|\boldsymbol{\varepsilon}_2\|^2}{\|\boldsymbol{e}\|^2} - \frac{v^2\|\boldsymbol{e}\|}{4\lambda_{\max}(\boldsymbol{k}_s)}\right)\|\boldsymbol{e}\|^2 \end{aligned} \tag{49}$$

According to (49), the differential form of the Lyapunov function can always be negative by selecting the appropriate controller gain matrices so the system is asymptotically stable.

5. Experimental Results

The method proposed in this work is based on the multi-DOF hydraulic manipulator experimental platform to carry out the experimental verification work shown in Figure 2.

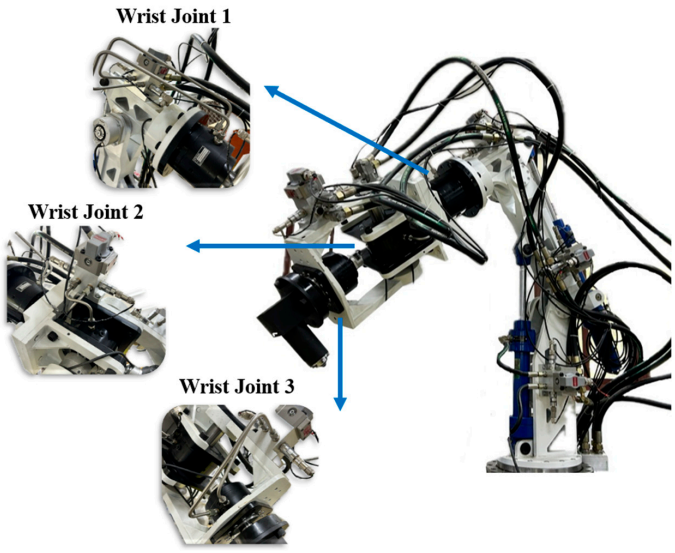


Figure 2. Multi-DOF hydraulic manipulator experimental platform.

5.1. Experimental Details

In this experimental platform, the wrist joints are driven by three hydraulic motors, among which the motors are vane-type swing hydraulic motors independently designed by the laboratory. The servo valves of each joint are Moog-G761 series, the maximum rated flow is 75 L/min, the maximum working pressure is 315 bar, and the 100% step response is 4–16 ms. The angle encoders are the Heidenhain-ERN-480 series whose line count is 5000. The measurement and control software was independently developed by the research team based on C++ language environment, with a 16-bit analog/digital (A/D) transition board Advantech PCI-1716 collects the pressure signals, a 16-bit counter card Heidenhain IK-220 collects the angle signal of the joints, and a 16-bit digital/analog (D/A) transition board Advantech PCI-1723 sends the control signal generated by the industrial control computer to the servo valves in each joint. The sampling interval is 1 ms. The velocity is produced by the backward difference of a high-accuracy angle signal. Meanwhile, a second-order Butterworth filter whose cutoff frequency is 50 Hz can be adopted to attenuate the measurement noise in the angle velocity signals.

The parameters of the experimental platform are shown in Table 1. The control flow chart of the experimental platform is shown in Figure 3. Firstly, the angle data of the joint are collected by the angle encoder of each joint, and the sensor electrical signal is converted into the actual angle value through the signal conditioning system (SCS). Then, the angle value is generated by the industrial control computer and sent to the servo valve through the SCS. Finally, position control is achieved by changing the flow rate of the servo valve.

Table 1. Parameters of the experimental platform.

Parameter	Value	Parameter	Value	Parameter	Value
m_1	75.9419 (kg)	m_2	44.4310 (kg)	m_3	15 (kg)
x_{c1}	1.9308×10^{-2} (m)	x_{c2}	0.1906 (m)	x_{c3}	3.2535×10^{-8} (m)
y_{c1}	-1.0589×10^{-2} (m)	y_{c2}	-5.4630×10^{-4} (m)	y_{c3}	-1.9696×10^{-8} (m)
z_{c1}	\	z_{c2}	-4.4235×10^{-2} (m)	z_{c3}	0.4609 (m)
l_1	0 (m)	l_2	0 (m)	l_3	\
I_{xx1}	\	I_{xx2}	2.9277 (kg·m^2)	I_{xx3}	5.7966 (kg·m^2)
I_{yy1}	\	I_{yy2}	0.9427 (kg·m^2)	I_{yy3}	5.7966 (kg·m^2)
I_{zz1}	0.9758 (kg·m^2)	I_{zz2}	2.0978 (kg·m^2)	I_{zz3}	0.2340 (kg·m^2)
k_{t1}	3.9686×10^{-8}	k_{t2}	3.9686×10^{-8}	k_{t3}	3.9686×10^{-8}
D_{m1}	1.4×10^{-4} (m^3/rad)	D_{m2}	1.0×10^{-4} (m^3/rad)	D_{m3}	6.72×10^{-5} (m^3/rad)
V_{011}	1.5882×10^{-4} (m^3)	V_{012}	9.5993×10^{-5} (m^3)	V_{013}	6.4507×10^{-5} (m^3)
V_{021}	1.5882×10^{-4} (m^3)	V_{022}	9.5993×10^{-5} (m^3)	V_{023}	6.4507×10^{-5} (m^3)
P_s	70 (bar)	P_r	2.6 (bar)	β_e	7×10^8
C_t	7×10^{-12}				

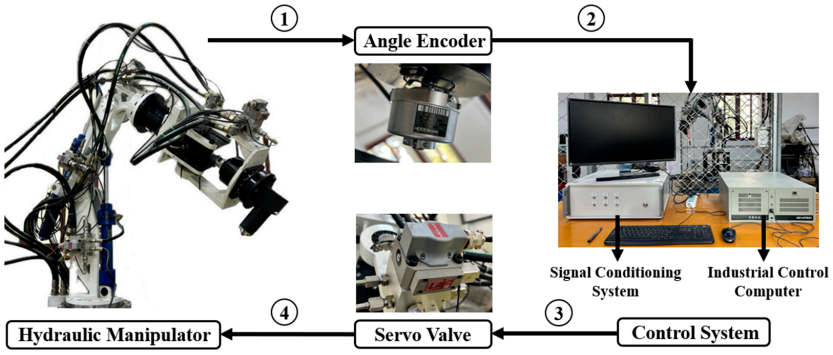


Figure 3. Control flow chart of the experimental platform.

The desired trajectories for each joint are as follows:

$$x_{1di} = 15 \times \sin(0.1\pi \times t) \times \left(1 - e^{-0.01 \times t^3}\right),\ i = 1, 2, 3 \tag{50}$$

In the experiment, a total of five controllers are designed for comparative analysis. The specific parameters of each controller are as follows:

(1) **ESO-ARISE (C1)**: This controller is used in this study. The control gains are selected as $\boldsymbol{k}_1 = \text{diag}\{160, 90, 240\}$, $\boldsymbol{k}_2 = \text{diag}\{160, 80, 220\}$, $\boldsymbol{k}_3 = \text{diag}\{160, 100, 220\}$, $\boldsymbol{k}_{r1} = \text{diag}\{30, 2, 80\}$, $\boldsymbol{k}_{r2} = \text{diag}\{30, 15, 80\}$, $\boldsymbol{k}_s = \text{diag}\{30, 2, 80\}$, $\boldsymbol{\beta}_1 = [15, 10, 50]^T$, $\boldsymbol{\beta}_2 = [15, 10, 50]^T$, $\boldsymbol{\Gamma}_1 = \text{diag}\{20, 10, 10\}$, $\boldsymbol{\Gamma}_2 = \text{diag}\{10, 10, 10\}$, $\boldsymbol{w}_{e1} = \text{diag}\{60, 10, 10\}$, $\boldsymbol{w}_{e2} = \text{diag}\{60, 10, 10\}$, $\boldsymbol{\beta}_{\min} = [0, 0, 0]^T$, and $\boldsymbol{\beta}_{\max} = [100, 100, 100]^T$.

(2) **ARISE (C2)**: This controller cancels the ESO estimation compensation for unmodeled uncertainties, leaving no $\boldsymbol{w}_{e1}$ and $\boldsymbol{w}_{e2}$ as the control gains, and other gains coefficients are consistent with the ESO-ARISE controller.

(3) **RISE (C3)**: This controller cancels the parameter's adaptive of the controller gains; the control gains do not have $\boldsymbol{\Gamma}_1$ and $\boldsymbol{\Gamma}_2$, and the other gains are consistent with ARISE.

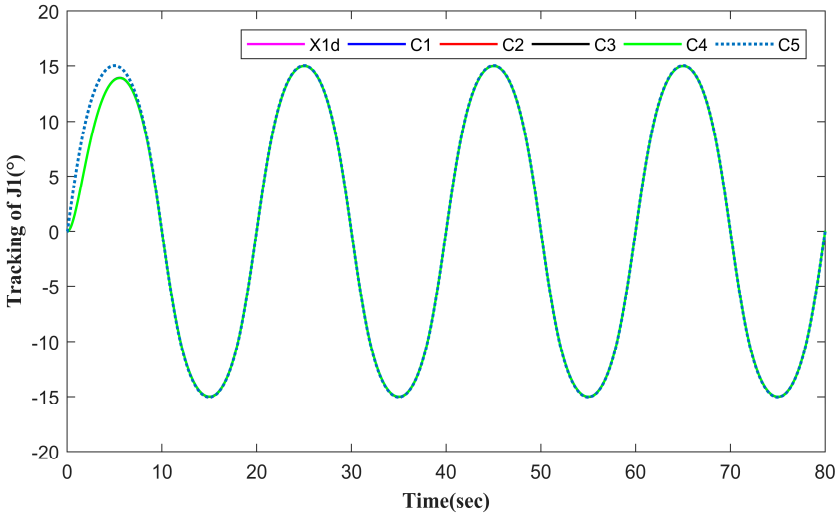
(4) **FLC (C4)**: This is the feedback linearization controller. The controller gains are only $\boldsymbol{k}_1$, $\boldsymbol{k}_2$, and $\boldsymbol{k}_3$, and the values of the gains are consistent with RISE.

(5) **PI (C5)**: This is a widely used controller in industries. The controller gains are chosen as $\boldsymbol{k_p} = \text{diag}\{6, 2, 25\}$ and $\boldsymbol{k_i} = \text{diag}\{2, 3, 8\}$.

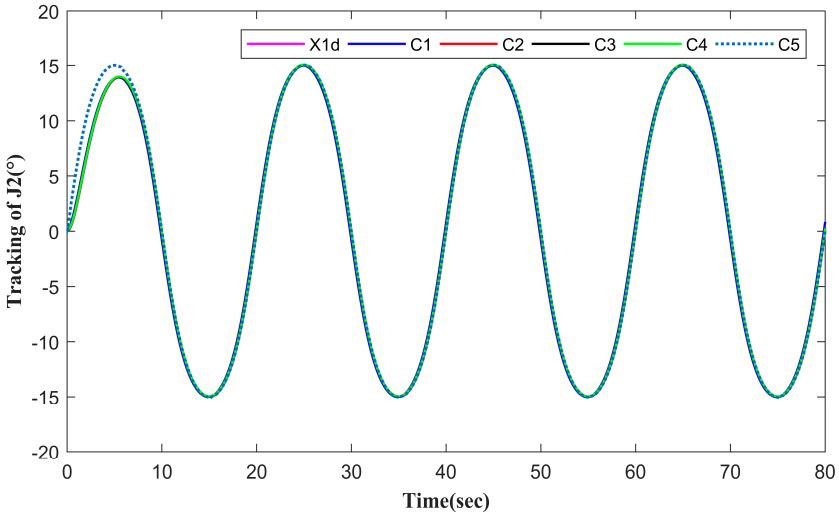
5.2. Experimental Results and Analysis

The comparison results of each controller are shown in the following figures. Among them, Figure 4 shows the results of tracking the command trajectory for different joints. Figures 5–7, respectively, represent the tracking error curves of wrist joints 1, 2, and 3 under different controllers. For ease of analysis, diagram (b) of each figure represents the locally enlarged figure from the beginning to 10 s during the experiment. Meanwhile, diagram (a) in Figure 8,Figure 9,Figure 10 represents the adaptive curves of the parameters of each joint, respectively, and diagram (b) represents the estimated curves of the disturbances of each joint, respectively. The diagrams of some manipulators with important postures are shown in Figure 11. Table 2 represents the root mean square (RMS) values for each controller. To facilitate analysis and expression, let C1-C2 represent the amount by which the RMS value of controller C1 has improved compared to C2.

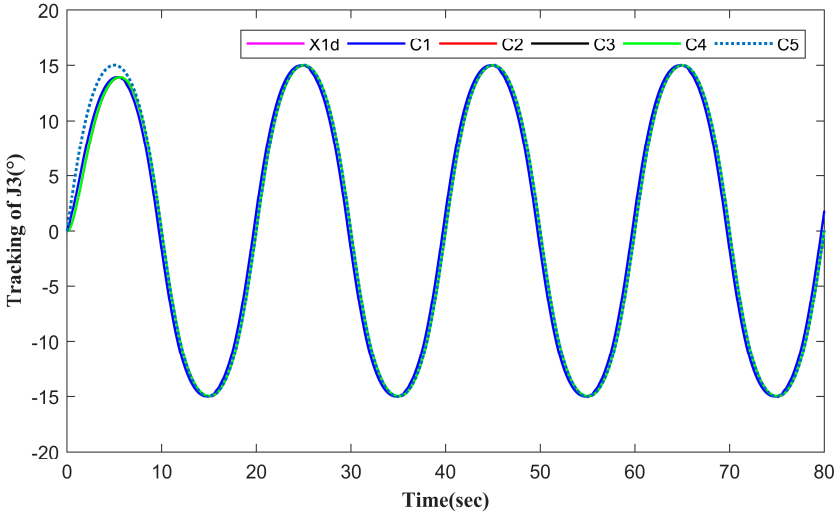
In Figure 4, it can be seen that the control performance of the C5 is significantly worse than the other controllers. From Figure 5, it can be observed that the tracking performance of controller C1 is significantly better than the other four controllers. Moreover, it effectively suppresses the impact caused by factors such as friction during the hydraulic motor reversal process. Combined with RMS value analysis, C1C2: 67.81%, C1–C3: 75.44%, C1–C4: 77.24%, and C1–C5: 90.73%. The same conclusion can be drawn from Figure 6. However, since wrist joint 2 is mainly responsible for the pitch motion of the wrist, it experiences larger torque variations, leading to relatively lower absolute tracking accuracy compared with joints 1 and 3. Considering the analysis of the RMS values, C1–C2: 82.88%, C1–C3: 83.07%, C1–C4: 87.54%, and C1–C5: 88.45%. In Figure 7, it can be observed that due to joint 3 being located at the end and having the smallest inertia, as well as experiencing the least inertia variations caused by loads during motion, the control performance of all controllers is superior to the other joints. Additionally, the observer compensation and parameter adaptive strategies do not show significant improvement in the control performance compared with other joints. The results from the RMS values indicate that C1–C2: 4.04%, C1–C3: 9.32%, C1–C4: 9.70%, and C1–C5: 13.36%.



(**a**)

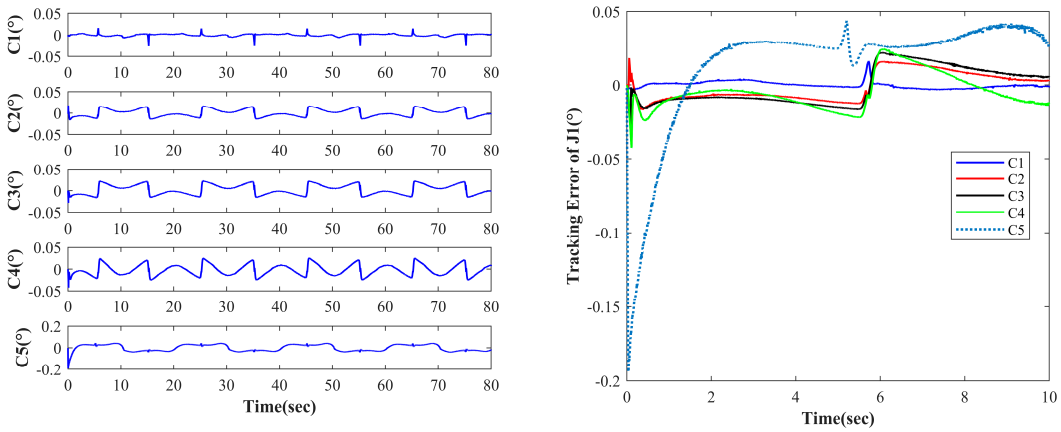


(**b**)



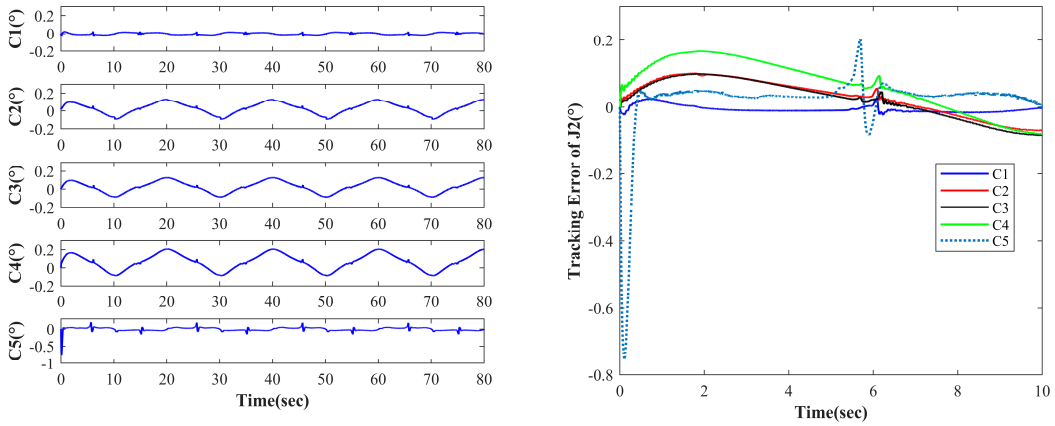
(**c**)

Figure 4. Tracking diagram of wrist joint under different controllers: (**a**) comparison of tracking diagram of joint 1; (**b**) comparison of tracking diagram of joint 2; (**c**) comparison of tracking diagram of joint 3.



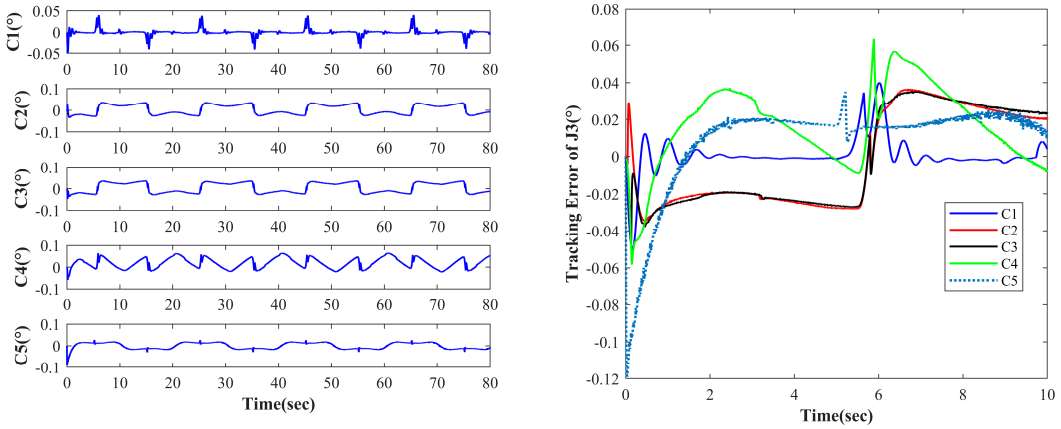
(**a**) (**b**)

Figure 5. Tracking error diagram of joint 1 under different controllers: (**a**) comparison of tracking errors between different controllers; (**b**) the tracking error comparison diagram of each controller for the first 10 s in the experiment.



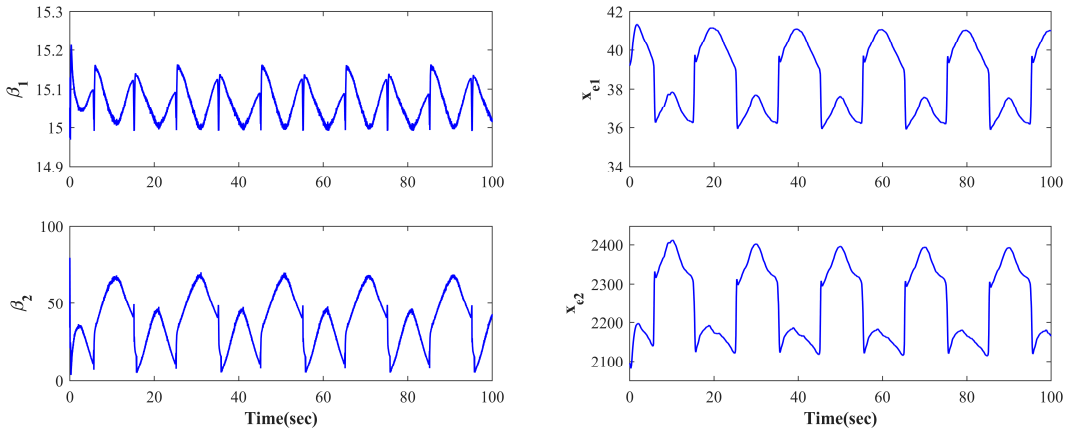
(**a**) (**b**)

Figure 6. Tracking error diagram of joint 2 under different controllers: (**a**) comparison of tracking errors between different controllers; (**b**) the tracking error comparison diagram of each controller for the first 10 s in the experiment.



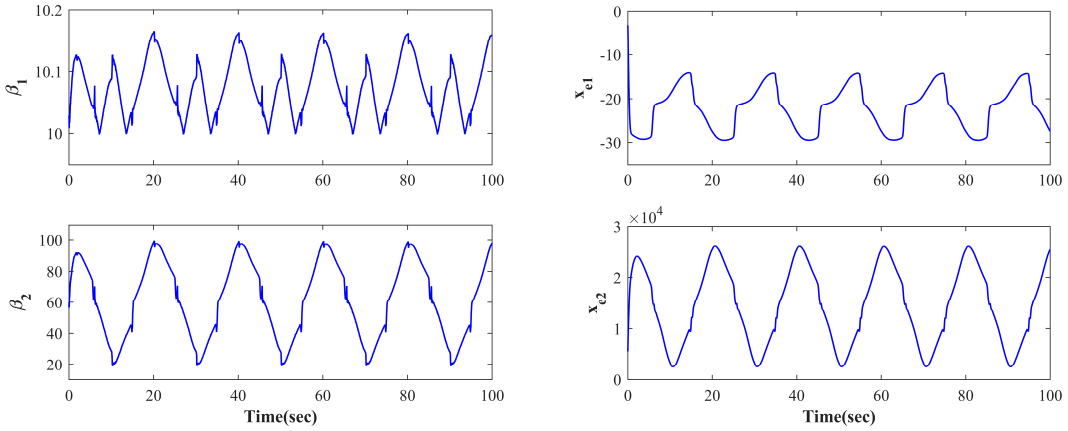
(**a**) (**b**)

Figure 7. Tracking error diagram of joint 3 under different controllers: (**a**) comparison of tracking errors between different controllers; (**b**) the tracking error comparison diagram of each controller for the first 10 s in the experiment.



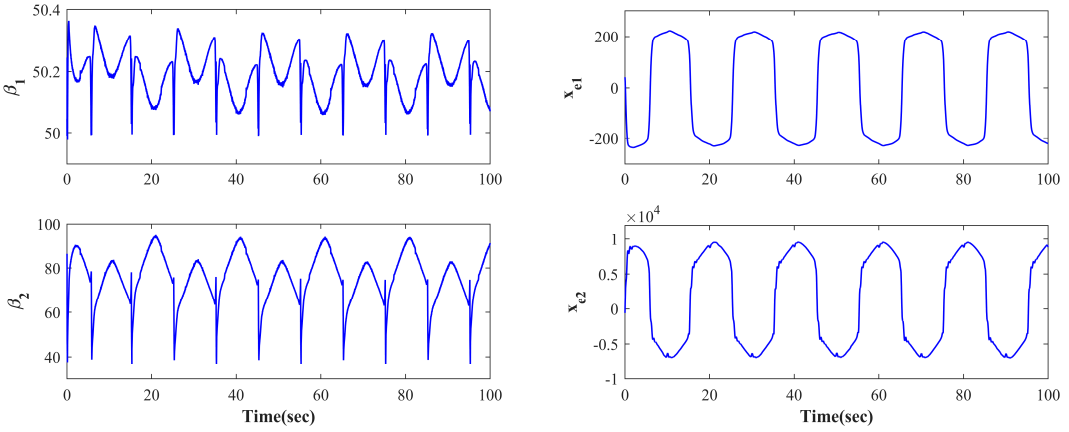
(**a**) (**b**)

Figure 8. Parameter estimators and state estimators for joint 1: (**a**) parameter estimators; (**b**) state estimators.



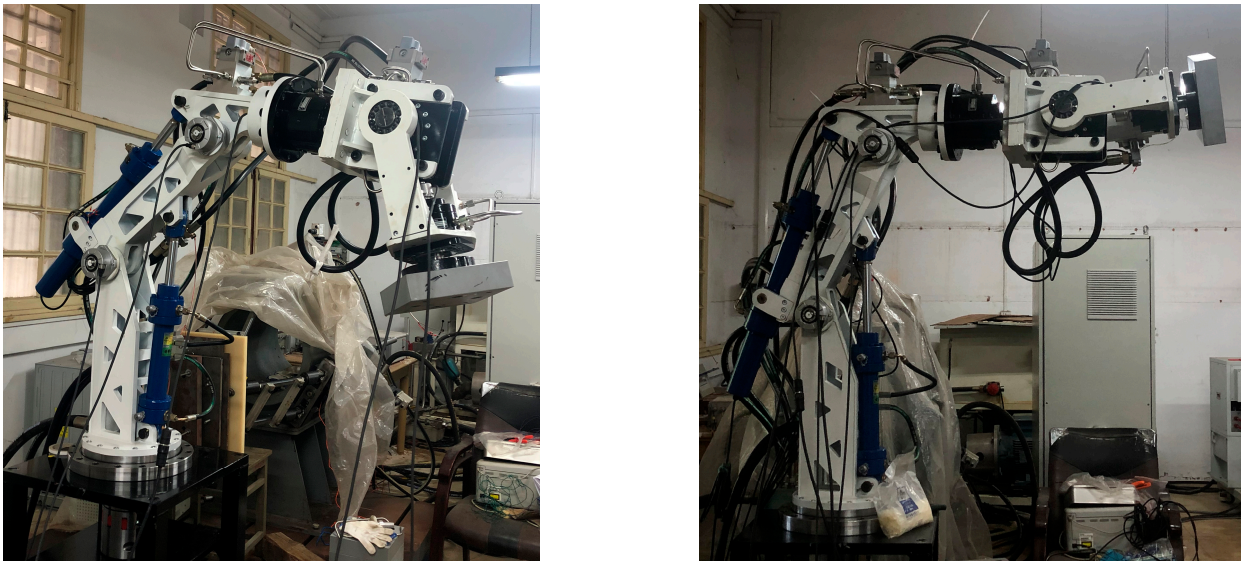
(**a**) (**b**)

Figure 9. Parameter estimators and state estimators for joint 2: (**a**) parameter estimators; (**b**) state estimators.



(**a**) (**b**)

Figure 10. Parameter estimators and state estimators for joint 3: (**a**) parameter estimators; (**b**) state estimators.



(**a**) (**b**)

Figure 11. Some key positions of the manipulator reached during the experiment: (**a**) All joints move to the lowest point of the desired trajectory; (**b**) All joints move to the highest point of the desired trajectory.

Table 2. The root mean square (RMS) value of each joint under different controllers.

Controller	Joint 1	Joint 2	Joint 3
C1	0.0028	0.0108	0.0214
C2	0.0087	0.0631	0.0223
C3	0.0114	0.0638	0.0236
C4	0.0123	0.0867	0.0237
C5	0.0302	0.0935	0.0247

From Figures 8–10, it can be observed that due to the effect of the $\mathrm{Proj}_*(\bullet)$ function, the parameter adaptive strategy remains within the estimated range. At the same time, because friction is not compensated for in the model compensation term, the curve of the state estimation resembles the friction curve.

6. Conclusions

In this work, we propose a method to utilize the ESO to observe the disturbance terms of a hydraulic manipulator and apply an adaptive strategy to estimate the parameters of the RISE controller. Firstly, the state-space equations of 3-DOF wrist joints considering hydraulic characteristics are established. Then, an ESO is designed based on the proposed model to estimate the disturbance terms for both matched and unmatched uncertainties. Due to the strong coupling between the robot joints and the strong nonlinearity of the hydraulic system, a nonlinear control law is designed using the RISE control technique and combined with adaptive theory to achieve parameter adaptation of the controller. Finally, the estimated disturbance terms from the ESO are compensated in the designed control law, and the global asymptotic stability of the system is proven based on Lyapunov function analysis. This work focuses on the wrist joints of a 6-DOF hydraulic manipulator, where industrial control computers are used to collect and send command signals, demonstrating the practical application of the proposed method. By comparing with four other control strategies, the proposed control strategy shows a significantly improved tracking performance for the command signals, further validating the feasibility of this method in hydraulic manipulator systems. At the same time, from the aspect of control strategy, it provides a solution for the wide application of heavy-duty hydraulic manipulators in the

industrial field under a hazardous working environment. However, at the same time, the method also has some limitations, the most important is that there are more controller parameters, and the process of adjusting the parameters during the experiment is too long. In future work, the plan is to combine position control and posture control to achieve high-precision servo control within the workspace of the 6-DOF hydraulic manipulator.

Author Contributions: Conceptualization, J.M., W.D. and J.Y.; methodology, J.M. and W.D.; software, J.M. and X.L.; validation, J.M., W.D. and X.L.; formal analysis, J.M.; investigation, W.D. and J.Y.; resources, W.D. and J.Y.; data curation, J.M. and X.L.; writing—original draft preparation, J.M.; writing—review and editing, W.D. and J.Y.; visualization, J.M. and W.D.; supervision, W.D. and J.Y.; project administration, J.Y.; funding acquisition, W.D. All authors have read and agreed to the published version of the manuscript.

Funding: xxxThis research was funded by the National Natural Science Foundation of China (No. 52275062) and the Natural Science Foundation of Jiangsu Province (BK20230096).

Data Availability Statement: If the reader has a reasonable request, the first author of this article may be contacted for the data presented in this article.

Conflicts of Interest: The authors declare no conflicts of interest.

Appendix A

In (1), the concrete expressions of the matrices $\boldsymbol{M}(\boldsymbol{q})$, $\boldsymbol{C}(\boldsymbol{q},\dot{\boldsymbol{q}})$, and $\boldsymbol{G}(\boldsymbol{q})$ are shown below:

$$\boldsymbol{M}(\boldsymbol{q}) = \begin{bmatrix} M_{11} & M_{12} & M_{13} \\ M_{21} & M_{22} & M_{23} \\ M_{31} & M_{32} & M_{33} \end{bmatrix} \tag{A1}$$

$$\begin{aligned} \boldsymbol{C}(\boldsymbol{q},\dot{\boldsymbol{q}}) &= \begin{bmatrix} B_{11} & B_{12} & B_{13} \\ B_{21} & B_{22} & B_{23} \\ B_{31} & B_{32} & B_{33} \end{bmatrix} \boldsymbol{B}(\dot{\boldsymbol{q}}) + \begin{bmatrix} D_{11} & D_{12} & D_{13} \\ D_{21} & D_{22} & D_{23} \\ D_{31} & D_{32} & D_{33} \end{bmatrix} \boldsymbol{D}(\dot{\boldsymbol{q}}) \\ \boldsymbol{B}(\dot{\boldsymbol{q}}) &= \begin{bmatrix} \dot{q}_2 & 0 & 0 \\ 0 & 0 & \dot{q}_1 \\ 0 & \dot{q}_3 & 0 \end{bmatrix}, \boldsymbol{D}(\dot{\boldsymbol{q}}) = \begin{bmatrix} \dot{q}_1 & 0 & 0 \\ 0 & \dot{q}_2 & 0 \\ 0 & 0 & \dot{q}_3 \end{bmatrix} \end{aligned} \tag{A2}$$

$$\boldsymbol{G}(\boldsymbol{q}) = \begin{bmatrix} G_1 \\ G_2 \\ G_3 \end{bmatrix} \tag{A3}$$

$$\begin{cases} M_{11} &= m_1\left(y_{c1}^2 + x_{c1}^2\right) + I_{zz1} \\ &\quad + m_2\left[z_{c2}^2 c_2^2 + z_{c2}^2 s_2^2 + \left(y_{c2}s_2 - x_{c2}c_2 - l_1\right)^2\right] + I_{xx2} + I_{yy2}c_2^2 \\ &\quad + m_3\left[z_{c3}^2 c_{23}^2 + z_{c3}^2 s_{23}^2 + \left(y_{c3}s_{23} - x_{c3}c_{23} - l_2c_2 - l_1\right)^2\right] + I_{xx3}s_{23}^2 + I_{yy3}c_{23}^2 \\ M_{12} &= m_2(-y_{c2}z_{c2}c_2 - x_{c2}z_{c2}s_2) \\ &\quad + m_3[(l_2s_3 - y_{c3})z_{c3}c_{23} - (l_2c_3 + x_{c3})z_{c3}s_{23}] \\ M_{13} &= m_3(-y_{c3}z_{c3}c_{23} - x_{c3}z_{c3}s_{23}) \\ M_{21} &= M_{12} \\ M_{22} &= m_2\left(y_{c2}^2 + x_{c2}^2\right) + I_{zz2} + m_3\left[\left(l_2s_3 - y_{c3}\right)^2 + \left(l_2c_3 + x_{c3}\right)^2\right] + I_{zz3} \\ M_{23} &= m_3\left[l_2x_{c3}c_3 - l_2y_{c3}s_3 + x_{c3}^2 + y_{c3}^2\right] + I_{zz3} \\ M_{31} &= M_{13} \\ M_{32} &= M_{23} \\ M_{33} &= m_3\left(x_{c3}^2 + y_{c3}^2\right) + I_{zz3} \end{cases} \tag{A4}$$

$$\begin{cases} B_{11} = 2m_2(y_{c2}s_2 - x_{c2}c_2 - l_1)(y_{c2}c_2 + x_{c2}s_2) + 2(I_{xx2} - I_{yy2})s_2c_2 \\ \quad +2m_3(-l_1 - l_2c_2 - x_{c3}c_{23} + y_{c3}s_{23})(l_2s_2 + x_{c3}s_{23} + y_{c3}c_{23}) \\ \quad +2(I_{xx3} - I_{yy3})s_{23}c_{23} \\ B_{12} = 2m_3(x_{c3}s_{23} + y_{c3}c_{23})(-l_1 - l_2c_2 - x_{c3}c_{23} + y_{c3}s_{23}) \\ \quad +2(I_{xx3} - I_{yy3})s_{23}c_{23} \\ B_{13} = 2m_3(y_{c3}z_{c3}s_{23} - x_{c3}z_{c3}c_{23}) \\ B_{21} = 0 \\ B_{22} = 0 \\ B_{23} = 2m_3[l_2c_3(l_2s_3 - y_{c3}) - l_2s_3(l_2c_3 + x_{c3})] \\ B_{31} = 0 \\ B_{32} = 0 \\ B_{33} = 0 \end{cases} \tag{A5}$$

$$\begin{cases} D_{11} = 0 \\ D_{12} = m_2(y_{c2}z_{c2}s_2 - x_{c2}z_{c2}c_2) \\ \quad +m_3[z_{c3}s_{23}(y_{c3} - l_2s_3) - z_{c3}c_{23}(x_{c3} + l_2c_3)] \\ D_{13} = m_3(y_{c3}z_{c3}s_{23} - x_{c3}z_{c3}c_{23}) \\ D_{21} = m_2[(l_1 - y_{c2}s_2 + x_{c2}c_2)(y_{c2}c_2 + x_{c2}s_2)] - (I_{xx2} - I_{yy2})s_2c_2 \\ \quad +m_3[(l_1 + l_2c_2 + x_{c3}c_{23} - y_{c3}s_{23})(l_2s_2 + x_{c3}s_{23} + y_{c3}c_{23})] \\ \quad -(I_{xx3} - I_{yy3})s_{23}c_{23} \\ D_{22} = 0 \\ D_{23} = m_3(-l_2y_{c3}c_3 - l_2x_{c3}s_3) \\ D_{31} = m_3(l_1 + l_2c_2 + x_{c3}c_{23} - y_{c3}s_{23})(x_{c3}s_{23} + y_{c3}c_{23}) - (I_{xx3} - I_{yy3})s_{23}c_{23} \\ D_{32} = m_3[l_2c_3(y_{c3} - l_2s_3) + l_2s_3(x_{c3} + l_2c_3)] \\ D_{33} = 0 \end{cases} \tag{A6}$$

$$\begin{cases} G_1 = 0 \\ G_2 = m_2g(x_{c2}c_2 - y_{c2}s_2) + m_3g(x_{c3}c_{23} - y_{c3}s_{23} + l_2c_2) \\ G_3 = m_3g(x_{c3}c_{23} - y_{c3}s_{23}) \end{cases} \tag{A7}$$

$$\begin{cases} s_i = \sin(q_i) \\ c_i = \cos(q_i) \end{cases} \tag{A8}$$

$$\begin{cases} s_{ij} = c_is_j + s_ic_j \\ c_{ij} = c_ic_j - s_is_j \end{cases} \tag{A9}$$

where m_i represents the mass of each link; x_{ci}, y_{ci}, and z_{ci} are the coordinates of the center of the link mass; I_{xxi}, I_{yyi}, and I_{zzi} represent the moment of inertia about the axis of the center of mass; and l_1 and l_2 are the distances along the X-axis of the link coordinate, and each link coordinate is fixed at the initial of the link. The specific method of link coordinate system modeling is referred to as the DH modeling method.

References

1. Jahnavi, K.; Sivraj, P. Teaching and learning robotic arm model. In Proceedings of the 2017 International Conference on Intelligent Computing, Instrumentation and Control Technologies (ICICICT), Kerala, India, 6–7 July 2017; pp. 1570–1575.
2. Lee, J.D.; Li, W.C.; Shen, J.H.; Chuang, C.W. Multi-robotic arms automated production line. In Proceedings of the 2018 4th International Conference on Control, Automation and Robotics (ICCAR), Auckland, New Zealand, 20–23 April 2018; pp. 26–30.
3. Sarkisov, Y.S.; Coelho, A.; Santos, M.G.; Kim, M.J.; Tsetserukou, D.; Ott, C.; Kondak, K. Hierarchical Whole-body Control of the cable-Suspended Aerial Manipulator endowed with Winch-based Actuation. In Proceedings of the 2023 IEEE International Conference on Robotics and Automation (ICRA), London, UK, 29 May–2 June 2023; pp. 5366–5372.
4. Axelson, S.; Kumar, K.S.P. Dynamic Feedback Linearization of a Hydraulic Valve-Actuator Combination. In Proceedings of the 1988 American Control Conference, Atlanta, GA, USA, 15–17 June 1988; pp. 2202–2203.
5. Du, H.; Shi, J.J.; Chen, J.D.; Zhang, Z.Z.; Feng, X.Y. High-gain observer-based integral sliding mode tracking control for heavy vehicle electro-hydraulic servo steering systems. *Mechatronics* **2021**, *74*, 102484. [CrossRef]
6. Su, D.H. Comparison of Electro-hydraulic Proportional Valve and Electro-hydraulic Servo Valve on Performances. *Hydraul. Pneum. Seals* **2008**, *4*, 2.

7. Zhou, M.L.; Yang, Z.G.; Gao, W.; Tian, Y.T.; Shen, C.L.; Li, P. Fuzzy control of a new type of piezoelectric direct drive electro-hydraulic servo valve. In Proceedings of the 2005 International Conference on Machine Learning and Cybernetics, Guangzhou, China, 18–21 August 2005; pp. 819–824.
8. Fang, Y.M.; Fan, Z.Y.; Ou, F.S.; Jiao, X.H. Multi-model switching control with input saturation for hydraulic servo system in rolling mill. *Control Theory Appl.* **2011**, *28*, 438–442.
9. Gu, W.W.; Yao, J.Y.; Yao, Z.K.; Zheng, J.Z. Robust Adaptive Control of Hydraulic System with Input Saturation and Valve Dead-Zone. *IEEE Access* **2011**, *6*, 53521–53532. [CrossRef]
10. Bu, F.P.; Yao, B. Nonlinear Adaptive Robust Control of Hydraulic Actuators Regulated by Proportional Directional Control Valves with Deadband and Nonlinear Flow Gains. In Proceedings of the 2000 American Control Conference, Chicago, IL, USA, 28–30 June 2000.
11. He, Z.X.; Feng, Y.B.; Liu, Y.; Li, L.; Ma, C.L.; Wang, H. Semi-physical real-time control of electro-hydraulic proportional position servo system based on Matlab/xPC. *J. Eng.* **2019**, *19*, 144–149. [CrossRef]
12. Chen, Z.; Helian, B.; Zhou, Y.; Geimer, M. An Integrated Trajectory Planning and Motion Control Strategy of a Variable Rotational Speed Pump-Controlled Electro-Hydraulic Actuator. *IEEE/ASME Trans. Mechatron.* **2023**, *28*, 588–597. [CrossRef]
13. Li, X.B.; Shang, Y.X.; Wu, S.; Jiao, Z.X. Dual valve controlled energy recovery EHA. In Proceedings of the CSAA/IET International Conference on Aircraft Utility Systems (AUS 2018), Guiyang, China, 19–22 June 2018; pp. 1495–1498.
14. Shi, Q.; Zhang, H. Robust FOPID controller design by GWO for position tracking of an EHA System. In Proceedings of the 2021 3rd International Conference on Industrial Artificial Intelligence (IAI), Shenyang, China, 8–11 November 2021; pp. 1–5.
15. Hwang, Y.L.; Ta, T.N.; Tran, C.S. Dynamic Analysis and Control of Hydraulic Machine System and Industrial Robotic Manipulators. *Appl. Mech. Mater.* **2018**, *883*, 1–7. [CrossRef]
16. Zhang, F.; Zhang, J.; Xu, B.; Zong, H. An Adaptive Robust Controller for Hydraulic Robotic Manipulators with a Flow-Mapping Compensator. *Int. J. Fluid Power* **2021**, *2*, 22. [CrossRef]
17. Yuan, Y.Q.; Sun, W.C. An Integrated Kinematic Calibration and Dynamic Identification Method with Only Static Measurements for Serial Robot. *IEEE/ASME Trans. Mechatron.* **2023**, *28*, 2762–2773. [CrossRef]
18. Mi, J.J.; Yao, J.Y. RISE-Based Adaptive Asymptotic Tracking Control of Space 3-DOF Manipulators with Hydraulic Actuators. In Proceedings of the 2023 42nd Chinese Control Conference (CCC), Tianjin, China, 24–26 July 2023; pp. 2813–2820.
19. Chen, Z.; Huang, F.H.; Chen, W.J.; Zhang, J.H.; Sun, W.C.; Chen, J.W.; Gu, J.S.; Zhu, S.Q. RBFNN-Based Adaptive Sliding Mode Control Design for Delayed Nonlinear Multilateral Telerobotic System with Cooperative Manipulation. *IEEE Trans. Ind. Inform.* **2020**, *16*, 1236–1247. [CrossRef]
20. Sun, H.; Huang, L.; He, L. Research on the Trajectory Tracking Control of a 6-DOF Manipulator Based on Fully-Actuated System Models. *J. Syst. Sci. Complex.* **2022**, *35*, 641–659. [CrossRef]
21. Li, P.; Yu, X.; Zhang, Y.M. The Design of Quasi-Optimal Higher Order Sliding Mode Control via Disturbance Observer and Switching-Gain Adaptation. *IEEE Trans. Syst. Man Cybern. Syst.* **2020**, *50*, 4817–4827. [CrossRef]
22. Zhang, H.J.; Fang, J.H.; Wei, J.H.; Yu, H.; Zhang, Q. Adaptive sliding mode control for tunnel boring machine cutterhead telescopic system with uncertainties. *Ind. Robot* **2023**, *50*, 162–173. [CrossRef]
23. Yao, B.; Bu, F.; Reedy, J.; Chiu, G.T.C. Adaptive robust motion control of single-rod hydraulic actuators: Theory and experiments. In Proceedings of the 1999 American Control Conference (Cat. No. 99CH36251), San Diego, CA, USA, 2–4 June 1999; pp. 759–763.
24. Zang, W.S.; Zhang, Q.; Su, J.P.; Feng, L. Robust Nonlinear Control Scheme for Electro-Hydraulic Force Tracking Control with Time-Varying Output Constraint. *Symmetry* **2021**, *13*, 2074. [CrossRef]
25. Xu, L.I.; Rui, G.C.; Yin, S.C.; Yu, T.; Gang, S. Adaptive Robust Control of Electro-hydraulic Position System Under Force Disturbance. *Manuf. Autom.* **2019**, *2*, 36–42.
26. Escorcia-Hernández, J.M.; Chemori, A.; Aguilar-Sierra, H. Adaptive RISE Feedback Control for Robotized Machining with PKMs: Design and Real-Time Experiments. *IEEE Trans. Control Syst. Technol.* **2023**, *31*, 39–54. [CrossRef]
27. Fischer, N.; Kan, Z.; Kamalapurkar, R.; Dixon, W.E. Saturated RISE Feedback Control for a Class of Second-Order Nonlinear Systems. *IEEE Trans. Autom. Control* **2014**, *59*, 1094–1099. [CrossRef]
28. Lei, X.S.; Zou, Y.; Dong, F. A composite control method based on the adaptive RBFNN feedback control and the ESO for two-axis inertially stabilized platforms. *ISA Trans.* **2015**, *59*, 424–433. [CrossRef]
29. Guo, B.Z.; Zhao, Z.L. On convergence of non-linear extended state observer for multi-input multi-output systems with uncertainty. *IET Control Theory Appl.* **2012**, *6*, 2375–2386. [CrossRef]
30. Liu, Z.W.; Huang, W. Linear active disturbance rejection control for hysteresis compensation based on backpropagation neural networks adaptive control. *Trans. Inst. Meas.* **2021**, *43*, 4. [CrossRef]

31. Hu, Y.F.; Li, D.H. An Improved Active Disturbance Rejection Controller for Hydraulic Valve-Controlled Hydraulic Motor. In Proceedings of the 2020 39nd Chinese Control Conference (CCC), Shenyang, China, 27–29 July 2020.
32. Laghridat, H.; Essadki, A.; Nasser, T. Coordinated control by ADRC strategy for a wind farm based on SCIG considering low voltage ride-through capability. *Prot. Control Mod. Power Syst.* **2022**, *7*, 7. [CrossRef]

Disclaimer/Publisher's Note: The statements, opinions and data contained in all publications are solely those of the individual author(s) and contributor(s) and not of MDPI and/or the editor(s). MDPI and/or the editor(s) disclaim responsibility for any injury to people or property resulting from any ideas, methods, instructions or products referred to in the content.